JOURNAL OF MAGNETIC RESONANCE IMAGING 30:1171–1178 (2009)

Original Research

Minimization of Nyquist Ghosting for Echo-Planar Imaging at Ultra-High Fields Based on a "Negative Readout Gradient" Strategy

Wietske van der Zwaag, PhD,[1,2]* José P. Marques, PhD,[1,2] Hongxia Lei, PhD,[1,2] Nathalie Just, PhD,[1,2] Tobias Kober, MSc,[1,3] and Rolf Gruetter, PhD[1,2,4]

Purpose: To improve the traditional Nyquist ghost correction approach in echo planar imaging (EPI) at high fields, via schemes based on the reversal of the EPI readout gradient polarity for every other volume throughout a functional magnetic resonance imaging (fMRI) acquisition train.

Materials and Methods: An EPI sequence in which the readout gradient was inverted every other volume was implemented on two ultrahigh-field systems. Phantom images and fMRI data were acquired to evaluate ghost intensities and the presence of false-positive blood oxygenation level-dependent (BOLD) signal with and without ghost correction. Three different algorithms for ghost correction of alternating readout EPI were compared.

Results: Irrespective of the chosen processing approach, ghosting was significantly reduced (up to 70% lower intensity) in both rat brain images acquired on a 9.4T animal scanner and human brain images acquired at 7T, resulting in a reduction of sources of false-positive activation in fMRI data.

Conclusion: It is concluded that at high B_0 fields, substantial gains in Nyquist ghost correction of echo planar time series are possible by alternating the readout gradient every other volume.

Key Words: Nyquist ghost; ghost correction; EPI; fMRI
J. Magn. Reson. Imaging 2009;30:1171–1178.

ECHO PLANAR IMAGING (EPI) is the most common sequence used for functional magnetic resonance imaging (fMRI) studies, allowing high temporal resolution (1). As the full *k*-space is acquired after a single RF-pulse using a train of reversals of the readout gradient, every alternate echo has to be time-reversed before applying the Fourier transform. Small inconsistencies between the odd and even *k*-space lines due to reversal of every other *k*-space line give rise to an image artifact known as the "Nyquist ghost," a ghost image shifted by half the field of view in the phase-encoding direction of the image.

The Nyquist ghost can in principle vary temporally in such a way that some coherence with the paradigm of an fMRI study is found, for example, through task-related motion. When this occurs, false-positive activation can be observed in areas affected by the Nyquist ghost. Where this ghost overlaps with the brain, false-positive activation may be difficult to distinguish from true activation. An effective Nyquist ghosting correction scheme is expected to reduce variability between scan sessions and to improve the trustworthiness of fMRI data.

Several ways of correcting for the Nyquist ghost artifact have been proposed. Typically, Nyquist ghost correction approaches in EPI are based on reference data, typically acquired in the absence of the blipped phase encode gradient (2,3). Numerous other methods have been suggested (4–7), but most have not become widely used in fMRI experiments, often because of a dependency on a separately acquired reference scan and increased sensitivity to motion and system instabilities. A promising route seems to be offered by parallel imaging-based techniques (8,9) where coil sensitivity information is used for ghost correction. While these approaches do not necessarily significantly impair signal-to-noise ratio (SNR) (10), the usage of acceleration factors is restricted, as for an effective acceleration factor of 3 in combination with a ghost correction scheme, the image SNR will be reduced by the g-factor corresponding to an acceleration of 6 in the phase-encoding direction, which is typically unwanted.

On clinical MR systems, a standard implementation of ghost correction is based on the acquisition of a

[1]Laboratory for functional and metabolic imaging, Ecole Polytechnique Fédérale de Lausanne, Switzerland.
[2]Department of Radiology, University of Lausanne, Switzerland.
[3]Siemens Switzerland, Advanced Clinical Imaging Technology, Lausanne, Switzerland.
[4]Department of Radiology, University of Geneva, Geneva, Switzerland.
Contract grant sponsor: Centre d'Imagerie BioMédicale (CIBM) of the UNIL, UNIGE, HUG, CHUV, EPFL, and Leenaards and Jeantet Foundations; Contract grant sponsor: SNF; Contract grant number: 3100A0 – 116220.
*Address reprint requests to: W.v.d.Z., CIBM, EPFL, Station 6, CH-1015 Lausanne, Switzerland. E-mail: wietske.vanderzwaag@epfl.ch
Received March 10, 2009; Accepted August 13, 2009.
DOI 10.1002/jmri.21951
Published online in Wiley InterScience (www.interscience.wiley.com).

couple of reference lines before the start of the actual *k*-space sampling. These lines can be acquired while the gradient waveform is played out a few times to ensure a stable *k*-space crossing and are thus minimally time-consuming. However, although a substantial ghost reduction is achieved, residual artifacts remain. Correcting for these residual Nyquist ghost artifacts becomes even more important at higher field strength, as the Nyquist ghosting increases with higher B_0 because the susceptibility-induced frequency variations which cause the Nyquist ghost become larger at higher B_0. Further artifact reduction is possible using a "negative gradient readout" strategy where a phase-encoded reference scan with reversed polarity of the readout gradient *(G_x)* is acquired at the beginning of the study (11).

The aim of the present study was to extend this method to time-series or fMRI data by continuously alternating the readout polarity of the echo planar acquisition, i.e. continuous acquisition of EPI volumes as usual in a standard fMRI experiment, but using readout gradient amplitudes of G_x and $-G_x$ in alternating volumes. This data acquisition method allows the application of several ghost correction schemes.

Nyquist ghosting can also form a significant problem in animal studies, due to the higher field strengths and smaller length scales typically used, resulting in larger susceptibility induced effects. Therefore, the ghost correction schemes were also tested on animal fMRI data acquired on a 9.4T small bore system.

THEORY

The equation describing the *k*-space signal for an EPI acquisition can be written as (11):

$$S(k_x,k_y)=\int\int m(x,y)\exp\left(2\pi i\left[\Delta f(x,y)\left(T_n+(-1)^n\left(\frac{k_x}{\gamma G_x}\right)\right)+k_x x+k_y y\right]\right)dxdy \quad (1)$$

where $m(x,y)$ represents the object's transverse magnetization, $\Delta f(x,y)$ the frequency shift distribution across the object, k_x and k_y the coordinates in *k*-space, and T_n the time at which the center of *k*-space line *n* is acquired. Terms related to eddy currents were not included because no dependence on k_y is expected and they are efficiently minimized using the manufacturer's ghost correction methods. Because Δf is mostly due to susceptibility-induced frequency shifts whose amplitude increases linearly with B_0, the inconsistencies between odd and even *k*-space lines, responsible for Nyquist ghosting, increase with the magnetic field strength. As Δf depends both on *y* and *x*, the inconsistencies between odd and even *k*-space lines of EPI data, responsible for the Nyquist ghost, depend on k_y and k_x (11), meaning that correction using a standard reference scan without phase encoding can be insufficient to remove all ghosting artifacts. Inverting the polarity of G_x amounts to a replacement of $(-1)^n$ with $(-1)^{n+1}$ in Eq. [1]. The readout gradients will be referred to here as "positive" and "negative" readout gradients, respectively (see Fig. 1). For simplicity, the concurrent datasets, whether in *k*-space or image space, will also be referred to as "positive" and "negative" data. All corrections were computed after the Fourier transform (FFT) along the readout dimension, denoted fft_x, was applied, but before application of the FFT in the phase-encode dimension, denoted fft_y. This space, where data are represented in x and k_y coordinates, as opposed to *k*-space (k_x, k_y) and image space (x,y), will be referred to as "projection space."

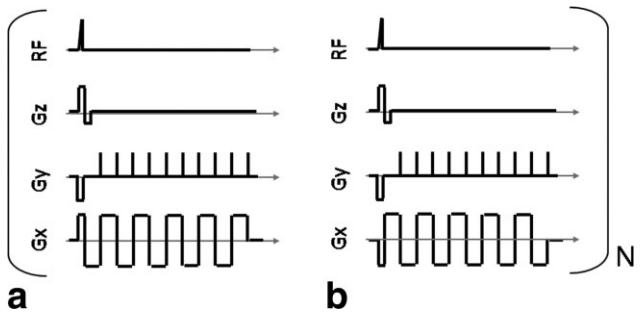

Figure 1. Sequence diagram of the modified EPI sequence. **a:** The normal, "positive" EPI volume. **b:** The volume with a reversed, "negative" readout. The pair is repeated throughout the fMRI acquisition train. On the 9.4T system the acquisition train was preceded by two nonphase-encoded reference scans, which are identical to the diagrams shown here, but without phase-encode blips.

To demonstrate the effectiveness of the alternate readout sampling strategy, three data-processing algorithms for ghost removal were implemented: A correction using the difference of the "projection space" phase of echo planar data pairs acquired with reversed readout gradients (2), which will be referred to as method "P"; a complex addition of the positive and negative readout gradient images, as suggested previously (12), referred to as method "A"; and finally a correction of the two images whereby the projection space phase of the complex addition is combined with the original amplitude part: "CP." These will be discussed in more detail below.

1. (P): After Fourier transformation in the read direction, fft_x, the phase difference between the "positive" and "negative" datasets was used to correct both by applying half of the phase difference to either dataset according to:

$$S(x,k_y)^+ = S(x,k_y)^+ e^{-i\Delta\varphi(x,k_y)/2} \text{ and}$$
$$S(x,k_y)^- = S(x,k_y)^- e^{+i\Delta\varphi(x,k_y)/2} \quad (2)$$

where S^+ and S^- represent the "positive" and "negative" datasets, respectively, in the projection space. $\Delta\varphi$ is the phase difference between the two datasets, still in the projection space, which can be calculated from:

$$\Delta\varphi(x,k_y) = angle\left(S(x,k_y)^+ / S(x,k_y)^-\right) \quad (3)$$

2. (A): After fft_x, the "positive" and "negative" images were added. Subsequently, fft_y was applied to create a single corrected image. Note that for this method the order of operations is of no consequence. For simplicity, the equations use the signal in *k*-space rather than image space. The summation of the "positive" and "negative" data in *k*-space results in the following signal equation:

$$S(k_x,k_y)=\int\int m(x,y)e^{2\pi i\left[\Delta f(x,y)T_n+k_x x+k_y y\right]}\left(e^{2\pi i\Delta f_{(x,y)}\left(\frac{k_x}{\gamma G_x}\right)(-1)^n}+e^{2\pi i\Delta f_{(x,y)}\left(\frac{k_x}{\gamma G_x}\right)(-1)^{(n+1)}}\right)dxdy \quad (4)$$

The term outside the brackets is the signal equation for EPI without the term reflecting distortions along the readout direction. The term inside the large brackets represents the ghost and can be simplified to:

$$\begin{aligned}&e^{2\pi i\Delta f_{(x,y)}\left(\frac{k_x}{\gamma G_x}\right)(-1)^n}+e^{2\pi i\Delta f_{(x,y)}\left(\frac{k_x}{\gamma G_x}\right)(-1)^{(n+1)}}\\&=2\cos\left(2\pi\Delta f_{(x,y)}\left(\frac{k_x}{\gamma G_x}\right)(-1)^n\right)\\&=2\cos\left(2\pi\Delta f_{(x,y)}\left(\frac{k_x}{\gamma G_x}\right)\right)\end{aligned} \quad (5)$$

As the $(-1)^n$ term disappears after summation, line-to-line inconsistencies are no longer present in *k*-space. However, the summation of the two complex numbers does result in a slight loss in SNR related to the amount of phase shift.

3. (CP): The phase resulting from (A), $\varphi_A(x,k_y) = angle(S(x,k_y)^- + S(x,k_y)^+)$, was combined with the amplitude of the "positive" or "negative" data to form two "Corrected Phase" datasets in the following way:

$$\begin{aligned}&S(x,k_y)^+=\left\|S(x,k_y)^+\right\|e^{i\varphi_A(x,k_y)}\text{ and}\\&S(x,k_y)^-=\left\|S(x,k_y)^-\right\|e^{i\varphi_A(x,k_y)}.\end{aligned} \quad (6)$$

In all three schemes, after phase correction, fft_y was applied to obtain data in image space.

Method CP is an integration of the two previous methods: In method A, an image where all line-to-line inconsistencies are corrected is obtained; from method P, it is known that the Nyquist ghost can be corrected by only removing the line-to-line phase inconsistencies in the projection space. Method CP uses the uncorrected magnitude signal in the projection space, as in method P, and the corrected projection space phase obtained through method A. Thus, temporal resolution is better retained than with method A. The difference between methods P and CP lies in the propagation of noise: In the presence of noise, method P will result in high variability where one of the two signals in the projection space is small, while method CP will be more robust.

MATERIALS AND METHODS

9.4T Data Acquisition

Data were acquired on an actively shielded 9.4T/31-cm (Inova, Varian, Palo Alto, CA) with 12-cm gradient (400 mT/m in 120 μs) using a quadrature ^{1}H RF-coil.

The manufacturer's implementation of the EPI sequence included acquisition of a single, nonphase-encoded volume with the same matrix size as the EPI, before the acquisition of the echo planar images.

The standard EPI sequence was modified to alternate the readout direction every other EPI volume as shown in Fig. 1. A second nonphase-encoded volume with inverted readout direction was also acquired following acquisition of the standard reference scan. This implementation differs from that of Hu and Le (11), where the readout train was shifted in time by one readout lobe in the first volume of the fMRI train.

In the manufacturer's implementation of the EPI sequence at 9.4T, a manually optimized tweaker gradient was used to balance the positive and negative gradient lobes, allowing all the echoes in the train to form at the center of their respective *k*-space lines. This optimization was applied separately for the "positive" and "negative" readout blocks to allow compensation for residual shim terms, present due to the large susceptibility changes in the rodent brain.

Images of a rat brain phantom consisting of an extracted brain from a P21 rat in a cylinder filled with gelatin were acquired to test the ghost correction schemes without the confounding influence of respiration-induced artifacts.

An fMRI study employing a forepaw stimulation task was done in the 9.4T system. Four male SD rats (≈300 g) were orally intubated and anesthetized with 2% isoflurane and stereotactically fixed with ear bars in a home-made holder. Throughout the experiments, animals were under α-chloralose anesthesia (≈26.7 mg/kg/h), continuously monitored and well-maintained under physiological conditions (rectal temperature 37.5°C, blood gas in pH ≈7.4 and pCO_2 ≈39 mmHg). The procedures were approved by the local ethics committee.

Following second-order shimming with FASTMAP (13), 300 volumes were acquired with a TE of 25 msec and a TR of 2 seconds. Each volume consisted of 10 slices with a matrix size of 64 × 64, field of view (FOV) of 25 × 25 mm^2, and a slice thickness of 1 mm. The employed block paradigm for fMRI consisted of a 30-second ON-period followed by 60 seconds OFF, repeated six times. The first two volumes in each train were reference scans acquired without phase-encode blips.

All images were corrected according to the manufacturer's implementation (2) using the scans acquired without phase encoding, providing the "comparison image." Further correction was done offline using MatLab (MathWorks, Natick, MA), applying methods P, A, and CP as described in the Theory section.

7T Data Acquisition

Data were acquired on an actively shielded 7T/68-cm (Siemens, Erlangen, Germany) with 41-cm head gradient coil and a TxRx volume RF-coil (InVivo, Pewaukee, WI). Permission for the study was obtained from the local ethics committee.

An EPI sequence that employed a sinusoidal readout gradient waveform shape (14) was modified to alternate the readout direction every other volume. In the manufacturer's implementation of the sequence, the acquisition of the echo planar train was preceded by the acquisition of three echoes sampled at the center line of *k*-space without phase-encoding, used to correct the phase difference between odd and even lines of the echo planar readout train.

Images of a 13-cm diameter oil phantom were acquired to test the ghost correction schemes without the confounding influence of respiration-induced artifacts.

Five subjects (three female) participated in an fMRI study employing a visual task consisting of a 12 Hz flashing checkerboard with 10 seconds ON, 20 seconds OFF, repeated eight times. Volumes of 20 transverse slices were acquired with a matrix size of 96 × 96 and the following scan parameters: FOV 192 × 192 mm^2, slice thickness 2 mm, slice gap 0.2 mm, TE 29 msec, TR 2.5 seconds. The quality of the shim was inspected visually after application of the vendors shim routine. When necessary, shimming was repeated. No fat-saturation was applied as this was not found to be necessary (14). fMRI studies were repeated with a nonalternating readout gradient for comparison. The same scan parameters were used as in the acquisition using the alternating readout gradient scheme.

Phase and magnitude images were saved for offline ghost correction processing in MatLab (MathWorks) as for the data acquired at 9.4T.

Data Analysis

Regions of interest (ROIs) were drawn in ghost, signal, and noise areas to calculate the ghost-to-signal ratio. The ghost-ROI was always drawn in the Nyquist ghost area outside the brain with the highest signal intensity. Typical ROIs are shown in Fig. 3. All ROIs covered ≈100 voxels.

Ghost signal intensity in the images was calculated following:

$$Ghost = \left(\frac{S_{ghost} - S_{noise}}{S_{signal}}\right) * 100 \qquad (7)$$

When comparing ghost levels in data corrected using method A to P or CP, it should be kept in mind that the noise level is lower by a factor $\sqrt{2}$ in data corrected with method A because of the temporal averaging.

The fMRI analysis was carried out for all data using FEAT (FMRI Expert Analysis Tool) v. 5.63, part of FSL (FMRIB's Software Library). The data were realigned, spatially and temporally smoothed before a General Linear Model (GLM) was formed with the blood oxygenation level-dependent (BOLD signal change modeled as a boxcar function convolved with the canonical hemodynamic response function (hrf). Subject motion up to half the voxel size was found and all data were retained for further processing. Z-score maps were obtained for the four processed datasets for each animal or subject. All maps were thresholded using clusters determined by $Z > 3.2$ and a (corrected) cluster significance threshold of $P < 0.05$. Ghost levels were then calculated in the fMRI data according to the equation given above.

In each dataset the activation found in the relevant part of the cortex was visually inspected. Also, data were examined for suspected false-positive activation in other parts of the cortex or outside the brain area. The number of active voxels was taken as an approximate measure of BOLD contrast-to-noise ratio in the fMRI datasets, as this is likely to reflect the sensitivity of the data to detect BOLD signal changes.

RESULTS

Simulations

To evaluate the influence of the ghost correction schemes on the temporal resolution of BOLD time-course data, the Nyquist ghost correction schemes were applied to synthetic fMRI data with TR = 2. fMRI data were modeled as a baseline with a BOLD signal change of 4% signal amplitude and a simultaneous 3% signal phase change, convolved with the default hrf from FLIRT (FSL). Durations of 20 seconds (block) and 0.2 seconds (event) were evaluated. BOLD amplitude time courses with and without correction are shown in Fig. 2A,C. The difference between the "true" time course and the corrected ones (Fig. 2B,D) is largest for method A and smallest for method CP. Thus, method CP is expected to yield a better conservation of the magnitude (BOLD-like) signal variations of the time series. However, correlation coefficients between the original time course and the time course after application of the correction schemes are larger than 99% for all three schemes for the block design. Even in the case of the event-related design, correlation coefficients of 98.2%, 94%, and 98.6% were found for methods P, CP, and A, respectively.

9.4T Data

EPI images of a rat brain phantom showed persistent but low-level ghosting, in this case of 6.5%, in the standard EPI magnitude image (Fig. 3, top row, leftmost). Applying the P and CP schemes resulted in a significant reduction to a ghosting level of 2.5%, while the images obtained with scheme A were virtually ghost-free.

When applying the three schemes to data from in vivo fMRI studies at 9.4T, all methods resulted in significant improvements in image quality as judged from an overall ≈60% reduction in ghosting levels (Table 1). When false-positive activation in the ghost region was detected, it was removed using schemes CP and A (Fig. 4). The substantial amount of false-positive activation was dramatically improved by ghost correction, and hence, increases in the maximum Z-score and number of active voxels were also significant (Table 1).

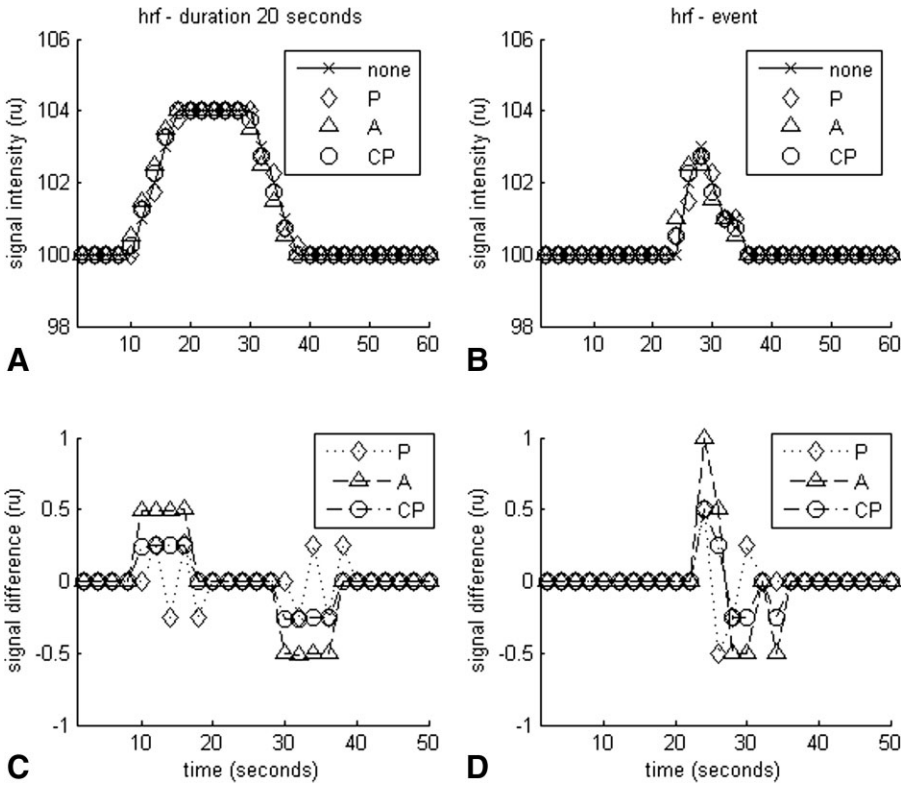

Figure 2. Simulation of an fMRI time course with TR = 2. BOLD signal change is modeled as a 4% increase in magnitude and 3% in phase during either 20 seconds (block) or 0.2 seconds (event). The uncorrected dataset represents the "true" BOLD signal. **A:** The block time course after application of each of the corrections. **B:** The differences between the "true" block BOLD signal and the time courses from ghost corrected data. **C:** Event time courses with and without corrections applied. **D:** The difference between "true" and corrected time courses in case of a short BOLD response.

7T Data

As with the 9.4T data, phantom data acquired at 7T showed consistent ghost artifacts (Fig. 3, bottom row). Without correction the measured ghost intensity was 10% and with correction schemes P, CP, and A this was reduced to 4%, 4%, and 2%, respectively. Note that the ghost had the highest intensity along the edges of the expected ghost area, over which the ROIs were drawn. Some Gibbs ringing was also visible, both in the corrected and uncorrected images, which was ascribed to the relatively small matrix of just 64 $\times$ 64 points, as well as the high SNR.

Identical slices taken from datasets of a representative human subject are shown in Fig. 5. Without correction, clearly discernable ghosting was detected. The average value over an ROI comparable to the one shown in Fig. 3 was 25%. Some distortions inside the brain ascribed to ghost–brain overlap were detected (see arrows in Fig. 4A) and largely reduced in the corrected datasets. Profiles taken through the area worst affected by the Nyquist ghost show the effect of ghost correction (see Fig. 4B). Significant amplitude reduction in the ghost areas is seen for all three corrected datasets relative to the uncorrected dataset, which is marked "none." Note the minimal reduction in signal

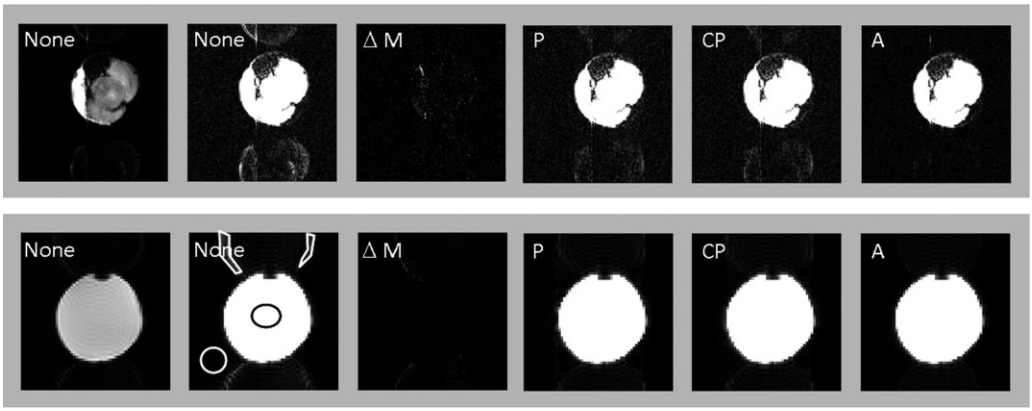

Figure 3. Phantom images. In the top row 9.4T data are shown; in the bottom row 7T data. Images presented furthest left are shown with normal scaling, other images were scaled to obtain identical noise amplitude and to make the Nyquist ghost visible. ΔM images show the mean difference in signal magnitude between 10 "positive" and 10 "negative" readout images. ΔPh images show the average difference in phase between 10 "positive" and 10 "negative" readout images. Examples of a noise, ghost, and signal ROI are shown in round white, shaped white, and round black shapes, respectively, on the 7T uncorrected data.

Table 1
9.4T fMRI Data, Correction Results

Method	Ghost intensity (mean ± SD)	Increase in # voxels "active" in SI	Average maximum Z-score
None	6.2 ± 2.3%	—	14.0 ± 0.7
P	3.1 ± 1.0%	Nonsignificant	13.9 ± 0.6
CP	2.4 ± 1.4%	40 ± 17%	15.5 ± 2.9
A	1.7 ± 0.7%	25 ± 14%	14.7 ± 2.7

Values are given as mean ± SD over animals.

intensity inside the brain area in the "A" dataset relative to the "none," "P" and "CP" datasets.

Nyquist ghost intensity measured before and after correction in the 7T data is summarized in Table 2. Ghosting levels in the 7T fMRI data were highly stable for the duration of the experiments. For all subjects, data acquired with inversion of the readout gradient, without application of the ghost-correction schemes (the data shown here as "none"), contained identical Nyquist ghost levels as data obtained with the standard EPI sequence (Table 2).

An example of activation maps generated from corrected and uncorrected data is shown in Fig. 6. The activation maps are displayed overlaid on one of the volumes of the fMRI train from which they were obtained. Note the excellent ghost reduction when using schemes CP and A. The white and black arrows indicate areas where false-positive activation was found in the ghost–brain overlap area. The white arrow indicates a sizable cluster of false-positive voxels that was notably absent in all of the Nyquist ghost-corrected datasets.

There was no significant change in the total number of voxels determined active between any of the fMRI sessions, as the detected false-positive clusters were relatively small compared to the primary active area in the occipital lobe. However, a nonsignificant increase in the number of voxels was found for data obtained by correction using scheme A.

However, in the front half of the brain a reduction in the number of "active" voxels of 17% and 26% compared to the uncorrected image was found in the data corrected with methods P and CP, respectively. This reduction is due to the elimination of small false-positive areas such as the one shown in Fig. 6. The datasets acquired without the alternating readout displayed the same ($P = 0.76$) number of "active" voxels in the brain as the noncorrected data acquired with the alternating readout gradient scheme.

DISCUSSION

In this study Nyquist ghost correction for echo planar time series data based on a continuous reversal of the EPI readout polarity was presented, utilizing three ghost correction schemes. Large improvements in Nyquist ghost levels were made without compromising the activation maps obtained from the fMRI data. Whenever, due to Nyquist ghosting, apparent activation outside the expected active brain region was found, this was removed or reduced when either ghost correction scheme "CP" or "A" was applied (see Figs. 4, 6).

Ghost removal was near-complete in phantom images, but less so in in vivo images, whether acquired in humans or animals (Tables 1, 2). Larger susceptibility differences in vivo, as well as respiration-induced frequency changes, may contribute to this difference.

Here it is assumed that the eddy currents need not be taken into account as, on most modern systems, any residual eddy currents are symmetrical for positive and negative gradient lobes. If this were not the case, a subtraction of phantom images acquired with positive and negative readout amplitude would yield a high intensity at the edges of the phantom. As can be seen in Fig. 3, this is not the case for either of the systems used here.

One possible source of artifacts for all of the above correction schemes is an appreciable change in signal between two acquisitions, which can result in a ghost representation of this change after correction. BOLD-induced phase or amplitude changes, however, tend to be relatively small, even at high magnetic fields, and slow, especially over the duration of a single TR. Phase changes and extremely large magnitude changes are typically restricted to large veins (15) which, at the high B_0 fields used in this study, yield very little signal, as TE $\gg$ $T_2{}^*_{venous}$ both at 9.4T in rats (16) and at 7T in humans (17). Since the duration of the hemodynamic response function usually spans several TR, it could be advantageous to use the mean of the preceding and succeeding images to determine the phase change. In principle, ghost correction could also be compromised by bulk motion, but this is in itself a reason to discard the fMRI data.

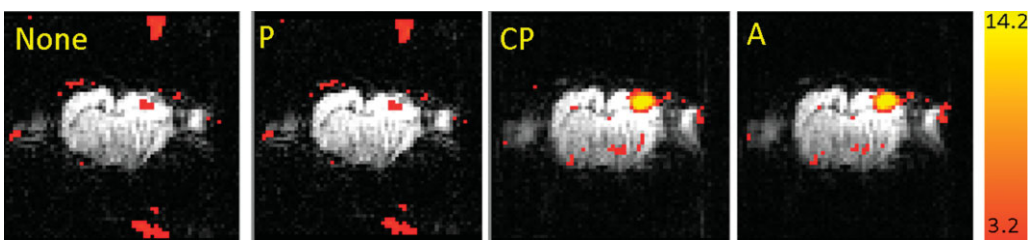

Figure 4. Representative slices taken from Z-score maps from 9.4T data calculated after ghost correction (cluster wise threshold of $P_{corr} < 0.05$) are shown overlaid on EPI images taken from the fMRI train. No brain extraction or other form of thresholding was applied to the echo planar images.

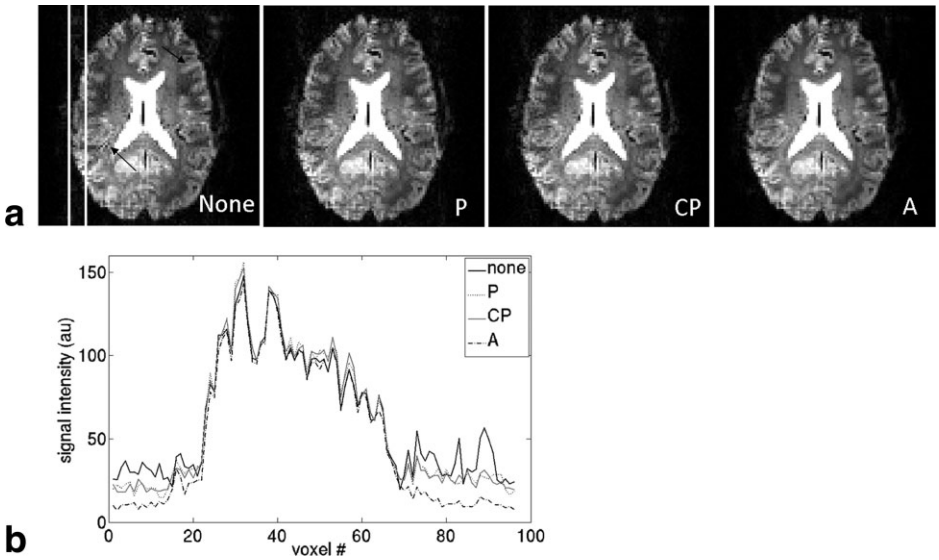

Figure 5. a: Slices taken from a representative 7T dataset. The arrows indicate areas where the ghost overlaps with the brain. When correction is applied the ghost intensity is reduced. **b:** Profiles averaged over the areas marked between the white lines are shown. Note that while all corrected data have lower signal intensity in the ghost area, only profiles taken from the P and CP datasets have higher signal intensity inside the brain than the uncorrected data.

As significant changes between scans can result in false-positive activation being found in the corrected datasets, all Z-score maps from corrected datasets were visually inspected for apparent activation shifted N/2 from the main foci of activation in the visual cortex. As no instances of such false-positive activation were detected in any of the datasets, we concluded that, in general, changes between volumes of an fMRI data train were sufficiently small for effective Nyquist ghost correction.

Implementation of any of the methods described requires minimal alteration of the pulse sequence, even when implemented on a clinical platform, and can easily be combined with *k*-space undersampling strategies such as parallel imaging or partial *k*-space acquisition, but since the correction is applied prior to FFT it is best implemented in the online data-processing software.

The application of the proposed schemes, as with any reference scan-based correction scheme, is only valid when the field inhomogeneities that cause the Nyquist ghost do not vary between acquisition of the reference scan and the image. Previously, the correction scan with a reversed readout gradient as proposed in Ref. 11 was acquired prior to the fMRI time-series, and thus the time between the acquisition of the reference scan and the images to be corrected was up to several minutes, or the whole duration of the fMRI experiment. In the correction schemes presented here the reference scans are an integral part of the fMRI acquisition train. Therefore, as the reference data are sampled throughout the entire experiment and data that are combined are acquired only TR seconds apart, the ensuing correction is almost insensitive to slow temporal drift such as system instabilities or subject motion.

While the application of scheme "A" results in almost complete removal of the Nyquist ghost, this comes at the expense of a convolution of the fMRI time course with a boxcar of width 2 and thus an effective reduction of the temporal resolution, which may be disadvantageous for fMRI studies requiring high temporal resolution. To compensate for this temporal filtering of the fMRI data, the model hemodynamic response function, hrf, was convolved with the same boxcar to adjust for the change in hrf, but this was not sufficient to counter the temporal smoothing effect caused by the summation technique and thus a, nonsignificant, increase in the number of active voxels was found after application of scheme A. Furthermore, using method A, the ghost is removed rather than corrected, and so a small loss in signal amplitude was found (as explained by Eq. [5]). This effect is visible in Fig. 5; while profiles from data "P" and "CP" have slightly higher signal intensity than the uncorrected data; a small decrease in signal was detected in the profile from data "A." In the case of substantial ghosting, some of the SNR loss may be recoverable by a sum of squares combination of image "A" and the "ghost" image shifted by half an FOV in the phase-encoding direction. The "ghost" image may be obtained through subtraction of the two uncorrected images that were summed to obtain image "A."

Another possibility for ghost removal in echo planar time series data acquired with the alternating readout gradient scheme is the application of a temporal filter, such as used in the UNFOLD method for partial *k*-space data (18). While application of such a filter would also incur a reduction in temporal resolution, it

Table 2
Ghosting Levels With and Without Correction in 7T Data

Method	Ghost intensity phantom data	Ghost intensity fMRI data
None	10.2%	18 ± 4%
P	4.1%	11 ± 3%*
CP	4.4%	11 ± 3%*
A	2.2%	5 ± 3%**
Unmodified acquisition		18 ± 5%

Values averaged over fMRI time courses and are given as mean ± SD over subjects.
*$P < 0.05$, **$P < 0.01$.

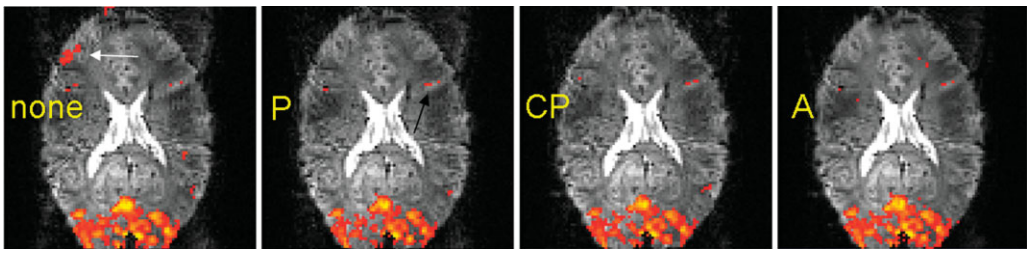

Figure 6. Representative slices from 7T Z-score maps obtained after ghost correction shown overlaid on a volume of the dataset they were calculated from. Z-score maps were thresholded using clusters determined by $Z > 3.2$ and a (corrected) cluster significance threshold of $P < 0.05$. The arrows indicate areas suffering from distortion and false-positive activation due to ghost-brain overlap in the uncorrected image.

may be advantageous for some applications, provided the Nyquist ghost is temporally stable.

The specific choice of the three presented ghost correction algorithms, or any other using the information offered by the alternating readout gradient scheme, may vary depending on the experiment in question. When averaging has to be performed, as in the case of arterial spin labeling (ASL) perfusion or diffusion experiments, the temporal smoothing of method A is inconsequential. However, for high temporal resolution fMRI data, the temporal smoothing in combination with a, though possibly minor, loss in SNR seems a reason to favor scheme P or CP. Method CP appears to have a slightly better performance with the removal of false-positive voxels in the functional maps. The difference any of the correction schemes can make depends on the quality of the fMRI dataset; while some Nyquist ghosting is always present and may be corrected for, false-positive activation or an absence of activation is not necessarily present. However, as this cannot be known until after the data are acquired, it may be advantageous to routinely employ the alternate readout acquisition scheme to allow application of one of the proposed Nyquist ghost-correction schemes.

In conclusion, efficient correction of the Nyquist ghost in EPI data is possible using readout gradient reversal throughout the time course of an fMRI experiment. While a complex summation of data acquired with an inverse readout gradient gives optimal Nyquist ghost removal and is suitable for applications requiring signal averaging, such as perfusion/diffusion, the correction schemes presented here as "CP" and "P" allow better conservation of the temporal resolution and are thus considered more suitable for fMRI.

REFERENCES

1. Mansfield P. Multiplanar image formation using NMR spin echoes. J Phys C 1977;10:L55–L58.
2. Bruder H, Fischer H, Reinfelder HE, Schmitt F. Image reconstruction for echo planar imaging with nonequidistant k-space sampling. Magn Reson Med 1992;23:12.
3. Reeder SB, Faranesh AZ, Atalar E, McVeigh ER. A novel object-independent "balanced" reference scan for echo-planar imaging. J Magn Reson Imaging 1999;9:847–852.
4. Chen NK, Wyrwicz AM. Removal of EPI Nyquist ghost artifacts with two-dimensional phase correction. Magn Reson Med 2004; 51:1247–1253.
5. Xiang QS, Ye FQ. Correction for geometric distortion and N/2 ghosting in EPI by phase labeling for additional coordinate encoding (PLACE). Magn Reson Med 2007;57:731–741.
6. Schmithorst VJ, Dardzinski BJ, Holland SK. Simultaneous correction of ghost and geometric distortion artifacts in EPI using a multiecho reference scan. IEEE Trans Med Imaging 2001;20: 535–539.
7. Zhang Y, Wehrli FW. Reference-scan-free method for automated correction of Nyquist ghost artifacts in echoplanar brain images. Magn Reson Med 2004;51:621–624.
8. Kellman P, McVeigh ER. Phased array ghost elimination. NMR Biomed 2006;19:352–361.
9. Kim YC, Nielsen JF, Nayak KS. Automatic correction of echo-planar imaging (EPI) ghosting artifacts in real-time interactive cardiac MRI using sensitivity encoding. J Magn Reson Imaging 2008;27:239–245.
10. de Zwart JA, van Gelderen P, Kellman P, Duyn JH. Application of sensitivity-encoded echo-planar imaging for blood oxygen level-dependent functional brain imaging. Magn Reson Med 2002;48: 1011–1020.
11. Hu X, Le TH. Artifact reduction in EPI with phase-encoded reference scan. Magn Reson Med 1996;36:166–171.
12. Mansfield P, Morris PG. NMR imaging in biomedicine. New York: Academic Press; 1982.
13. Gruetter R. Automatic, localized in vivo adjustment of all first- and second-order shim coils. Magn Reson Med 1993;29:804–811.
14. Speck O, Stadler J, Zaitsev M. High resolution single-shot EPI at 7T. Magma 2008;21:73–86.
15. Menon RS. Postacquisition suppression of large-vessel BOLD signals in high-resolution fMRI. Magn Reson Med 2002;47:1–9.
16. Lee SP, Silva AC, Ugurbil K, Kim SG. Diffusion-weighted spin-echo fMRI at 9.4 T: microvascular/tissue contribution to BOLD signal changes. Magn Reson Med 1999;42:919–928.
17. Peters AM, Brookes MJ, Hoogenraad FG, et al. T2* measurements in human brain at 1.5, 3 and 7 T. Magn Reson Imaging 2007;25: 748–753.
18. Madore B. Using UNFOLD to remove artifacts in parallel imaging and in partial-Fourier imaging. Magn Reson Med 2002;48: 493–501.